

Grid sensitivity and role of error in computing a lid-driven cavity problem

V. K. Suman,¹ Siva Viknesh S.,^{1,*} Mohit K. Tekriwal,¹ Swagata Bhaumik,² and Tapan K. Sengupta^{1,†}

¹*High Performance Computing Laboratory, Indian Institute of Technology Kanpur, Kanpur-208 016 India*

²*Department of Mechanical Engineering, Indian Institute of Technology Jammu, India*



(Received 3 August 2018; published 16 January 2019)

The investigation on grid sensitivity for the bifurcation problem of the canonical lid-driven cavity (LDC) flow results is reported here with very fine grids. This is motivated by different researchers presenting different first bifurcation critical Reynolds number (Re_{cr1}), which appears to depend on the formulation, numerical method, and choice of grid. By using a very-high-accuracy parallel algorithm, and the same method with which sequential results were presented by Lestandi *et al.* [Comput. Fluids **166**, 86 (2018)] [for (257×257) and (513×513) uniformly spaced grid], we present results using (1025×1025) and (2049×2049) grid points. Detailed results presented using these grids help us understand the computational physics of the numerical receptivity of the LDC flow, with and without explicit excitation. The mathematical physics of the investigated problem will become apparent when we identify the roles of numerical errors with the ambient omnipresent disturbances in real physical flows as interchangeable. In physical or in numerical setups, presence of disturbances cannot be ignored. In this context, the need for explicit excitation for the used compact scheme arises for a definitive threshold amplitude, below which the flow relaxes back to quiescent state after the excitation is removed in computations. We also implement the present parallel method to show the physical aspects of primary and secondary instabilities to be maintained for other numerical schemes, and we show the results to reflect the complex physics during multiple subcritical Hopf bifurcation. Also, we relate the various sources of errors during computations that is typical of such shear-driven flow. These results, with near spectral accuracy, constitute universal benchmark results for the solution of Navier-Stokes equation for LDC.

DOI: [10.1103/PhysRevE.99.013305](https://doi.org/10.1103/PhysRevE.99.013305)

I. INTRODUCTION

Traditionally fluid dynamical systems undergoing bifurcation or instability are classified as either amplifiers or oscillators. This classification is important as it represents two classes of canonical problems, namely: (i) The zero pressure gradient boundary layer (which requires explicit excitation to display flow instability and hence called an amplifier of disturbance) and (ii) vortex dominated flows (external flow past a cylinder and flow inside a LDC which do not require any excitation for moderate grids using nondissipative methods). The instability for amplifier is usually governed by linearized Navier-Stokes equation [1,2] and the instability and transition display spatiotemporal variations [3,4]. For the oscillators, it is assumed that the characteristic frequency is independent of background disturbances, and is fixed by a resonance mechanism, for it to be called as oscillator or resonator [5]. The present study focuses on the problem of two-dimensional (2D) LDC, acting as an oscillator. Here, we explore the computational physics aspects of Hopf bifurcation sequences and subsequent nonlinear dynamics of LDC using refined grids, which have not been used before.

The 2D flow in a square LDC (of side L) is used not only to develop newer methods for computing incompressible Navier-Stokes equation (NSE) due to its unambiguous

boundary conditions and simple geometry, but also to help us understand nonlinear dynamics of vortex-dominated unsteady flows. When the lid is given a constant translational speed (U), then for high Re ($=UL/\nu$, with ν as the kinematic viscosity), the flow becomes unsteady inside the cavity due to various disturbance sources present in the computation. A schematic of the problem is shown in Fig. 1, with two specific points marked, where the flow is explicitly excited (top left) and unsteady output sampled (top right). In high-accuracy computing, when the usual sources of errors due to discretization are minimized, unsteadiness still arises in LDC flow due to other sources of errors, which include aliasing error, Gibbs' phenomenon, etc., of which Gibbs' phenomenon is physical. This has been identified at the corners of the top lid in the pseudospectral computations of NSE [6,7]. However, as we are going to show that for inadequately resolved grid, aliasing error is distributed at all the points of the top lid. Computing LDC flow by other discrete computing methods [8–10] display unsteadiness at varying Re values. One can compute steady flow at low Re by various methods. At higher Re , the flow experiences bifurcation and displays unsteadiness. In Ghia *et al.* [9], results for a wide range of Re up to 10 000 are presented to be steady. Numerical results obtained by high-accuracy combined compact difference (CCD) schemes presented in Sengupta *et al.* [11,12] indicate creation of a transient polygonal vortex at the core, with permanent gyrating satellite vortices around it for $Re = 10\,000$ using a (257×257) uniform grid. The same sixth-order CCD scheme has been used in a sequential computing mode

*viknesh@iitk.ac.in

†tksen@iitk.ac.in

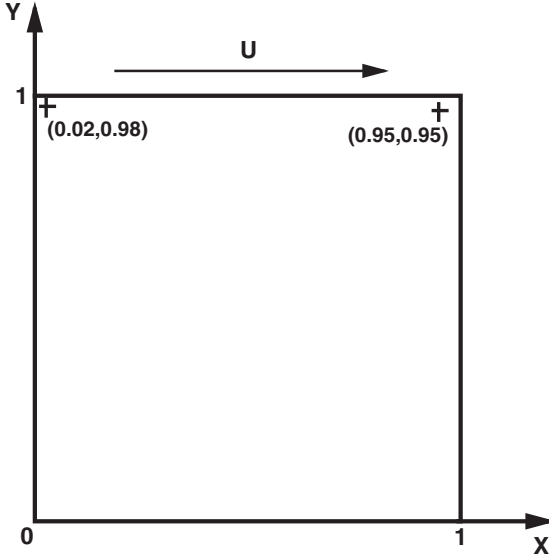


FIG. 1. The schematic of the computational domain and location of sampling point $(0.95,0.95)$ with vortical excitation applied at $(0.02,0.98)$ for a (257×257) grid.

[13] for (257×257) and (513×513) grids, for a range of super-critical Reynolds numbers to achieve the following: (i) Trying to reconcile critical Reynolds numbers for first bifurcation (Re_{cr1}) obtained by different numerical approaches to be in the same range and (ii) to show that for increasing Re following the first Hopf bifurcation, the flow in a limit cycle suffers a secondary instability. This requires computation of the flow field over a significantly longer time period. The first goal is met by exciting the flow field with a pulsating vortex inside the LDC. Here, these aspects are further investigated using (1025×1025) and (2049×2049) uniformly spaced grids, with focus on the threshold amplitude of excitation needed to trigger self-sustained unsteadiness in the cavity, when the excitation is removed for the (1025×1025) grid.

Use of lower-order methods in obtaining equilibrium flow results in contaminated eigenvalues for classical bifurcation studies. However, DNS of NSE [14–16] reveal that the flow loses stability via Hopf bifurcation with respect to increasing Re . Critical Re_{cr1} and frequencies obtained from DNS and eigenvalue analysis do not match and such differences are noted for different DNS results too, for various reasons explained here. It is shown that Re_{cr1} depends upon the accuracy of the method and how the flow is established in DNS [12,16,17]. Impulsively started flow is ideal to study the dynamics, as it triggers all frequencies at $t = 0$ [11–13]. These simulations are extremely sensitive to the accuracy of the method, so much so that parallelization of the code by Schwarz domain decomposition technique [18] does not allow one to reproduce the results obtained with sequential computing, despite having a large number of overlapping points at the subdomain boundaries. In the present work, we develop a new parallelization strategy (to be reported elsewhere), which does not require taking overlapping subdomains, while producing results which ensures reproduction of sequentially obtained results.

Unsteadiness for varying parameters are studied in bifurcation theory [19] caused by flow instabilities [2], with linear

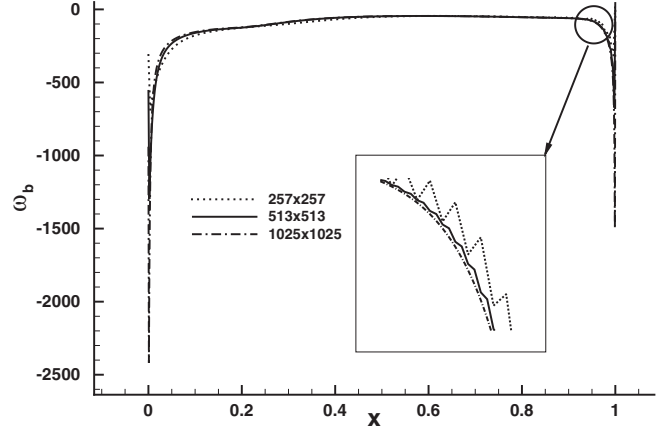


FIG. 2. Comparison of computed wall vorticity distribution— ω_b at the top wall for the LDC flow at $Re = 9600$ at time $t = 1750$ for (257×257) , (513×513) , and (1025×1025) grids.

instability of equilibrium flow and DNS have been used to evaluate Re_{cr1} , which provide scattered values for LDC flow. Auteri *et al.* [20] obtained Re_{cr1} , using a second-order projection method along with a second-order backward difference for time integration, to be between 8017.6 and 8018.8. The authors added that an analysis beyond first bifurcation led them to suppose that the system passes through a second Hopf bifurcation for a second critical Reynolds number located in the interval (9687, 9765). Various researchers also noted different value of Re_{cr1} : equal to 8031.93 in Sahin and Owen [21] and 7972 in Cazemir *et al.* [22] using a finite-volume method. Bruneau and Saad [23] noted this to be in the range of 8000 to 8050, without showing any relevant bifurcation diagram, while using (1024×1024) grid for third- and fifth-order spatial discretization method. However, the use of three time-level Gear method [23], produces spurious mode to affect global results. Also of interest are high-accuracy methods to report relatively higher values of Re_{cr1} . However, it is noted that very diffusive methods produce very high Re_{cr1} , by attenuating disturbances to delay unsteadiness [9,24,25].

CCD scheme has been used to explain multiple Hopf bifurcations [13,17]. Osada and Iwatsu [16] have identified Re_{cr1} value given by $7987 \pm 2\%$, obtained using compact scheme on nonuniform (128×128) and (257×257) grids. This value is based on a linear interpolation of data from two grids in Fig. 3 for u -component of velocity at the core of LDC [16]. The figure shows grid dependence of the computed results, as the equilibrium amplitude squared (A_e^2) versus Re curves have diverging slopes. Thus, these are grid-dependent results [16], as is also noted here between (257×257) and (513×513) grids. We will provide justification for such differences, while producing new insight about high-accuracy computing of oscillator type flows. Here all computations are obtained by starting from quiescent condition at $t = 0$.

There are also widely different Re_{cr1} reported [26], where Re_{cr1} is in the range of 10 000 to 10 500 obtained by regularizing the lid velocity (by removing corner singularities at the top lid) using compact scheme. As noted earlier, the onset of flow instability is due to distributed aliasing error causing grid-scale oscillation near the top lid. In addition, there is the Gibbs' phenomenon present at the corners of LDC, which

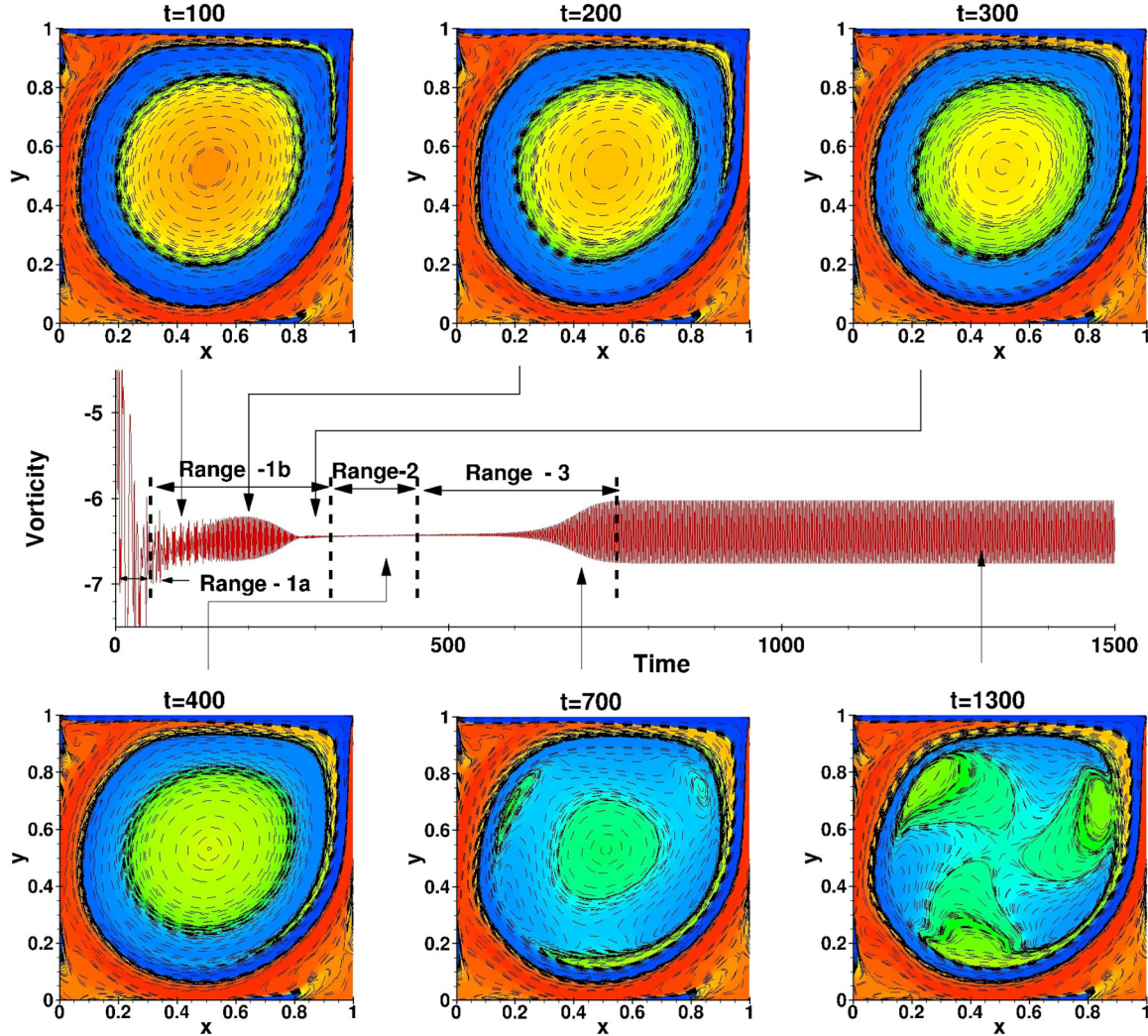


FIG. 3. Illustration of the vorticity dynamics at supercritical $Re = 8750$ for the LDC problem solved using a (257×257) grid. The plotted vorticity time series is sampled at $(0.95, 0.95)$. Vorticity contours plotted at the indicated times shows a well defined triangular vortex during transient stages.

is identical to such discontinuity in the actual flow. This is due to the fact that the corner points must have zero vorticity topologically, while the neighboring points will have high wall vorticity values. This discrete jump between the corner point with its neighbor gives rise to Gibbs' phenomenon. This is primarily present at the top corners, and regularizing the lid velocity can reduce the discrete jump, but cannot remove it altogether. Poliashenko and Aidun [27], however, reported a value of $Re_{cr1} = 7763 \pm 2\%$ using a commercial FEM package, which has sources of large numerical error. Peng *et al.* [28] reported a value of $Re_{cr1} = 7402 \pm 4\%$ using finite difference method by Marker and Cell (MAC) technique.

To obtain Re_{cr1} , DNS is preferred over eigenvalue analysis (which performs temporal analysis assuming all points to have identical time variation), while true spatiotemporal dynamics is traced in DNS. In the schematic in Fig. 1, vorticity time series is sampled at $(x = 0.95, y = 0.95)$. This point is preferred for analysis purpose [11–13,17].

Here, high-accuracy CCD scheme is used along with refined (1025×1025) and (2049×2049) grids without regularizing the lid velocity. To the knowledge of the authors, these

are the highest resolved simulations for 2D LDC problem provided with detailed analysis of nonlinear and error dynamics. As noted in Fig. 12 of Lestandi *et al.* [13], the two grids with (257×257) and (513×513) points produce different Re_{cr1} , even with subcritical excitation by a pulsating vortex placed at $(x = 0.02, y = 0.98)$. The threshold amplitude of excitation for subcritical Reynolds numbers are shown here to be different for different grid resolutions. This has been critically studied for all the grids used here.

II. GOVERNING EQUATIONS AND NUMERICAL METHODS

DNS of the 2D flow is carried out using the stream function-vorticity formulation of the NSE given by

$$\nabla^2 \psi = -\omega, \quad (1)$$

$$\frac{\partial \omega}{\partial t} + (\vec{V} \cdot \nabla) \omega = \frac{1}{Re} \nabla^2 \omega, \quad (2)$$

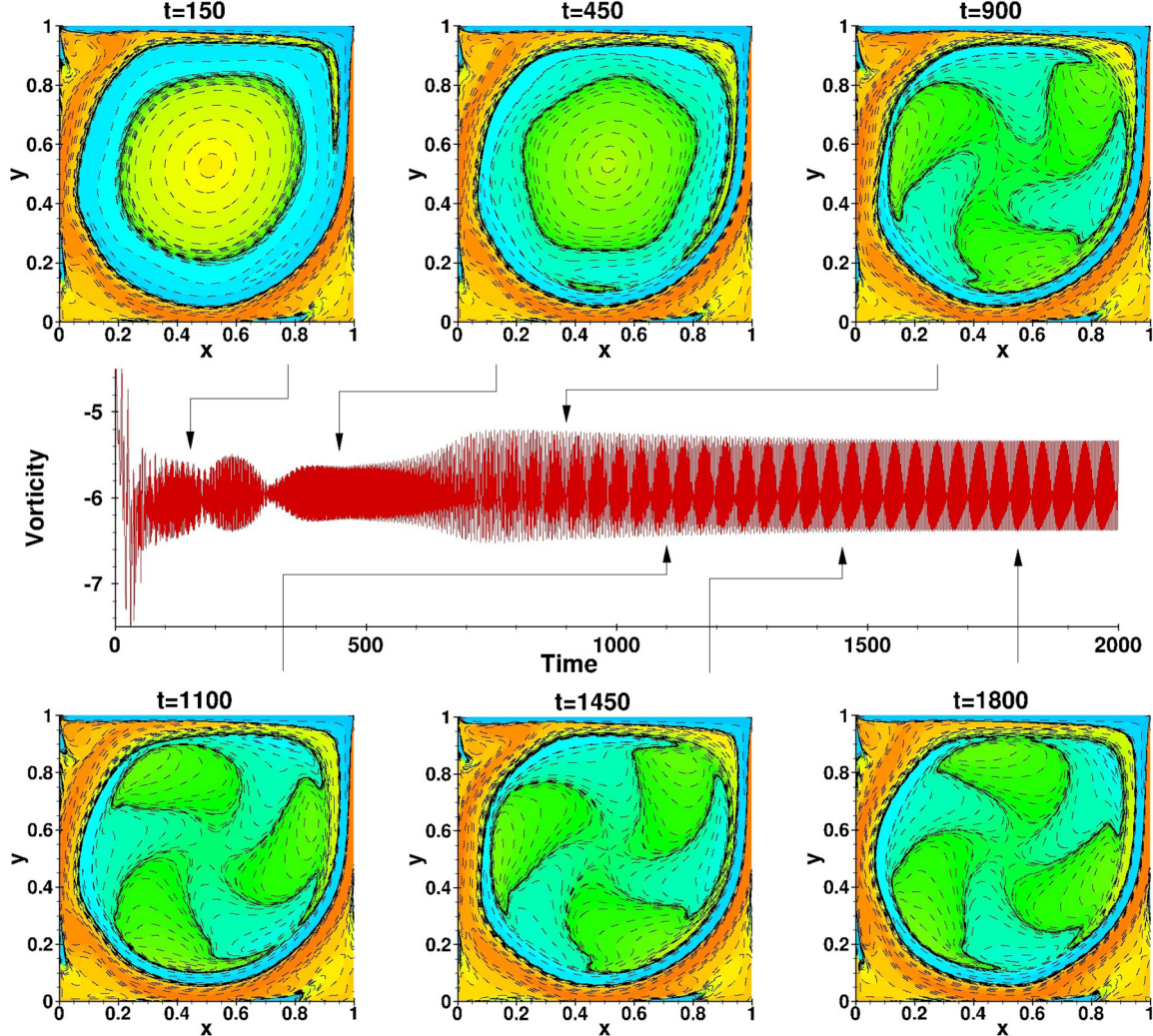


FIG. 4. Illustration of the vorticity dynamics at super-critical $Re = 9600$ for the LDC problem solved using a (1025×1025) grid. The plotted vorticity time series is sampled at $(x = 0.95, y = 0.95)$. Vorticity contours plotted at the indicated times show well defined pentagonal and triangular vortices during the transient stages.

where ω is the nonzero out-of-plane component of vorticity for the 2D problem. The velocity is related to the stream function by $\vec{V} = \nabla \times \vec{\Psi}$, where $\vec{\Psi} = [0 \ 0 \ \psi]$. The parameters L and U are also used as length and velocity scales, respectively, to nondimensionalize NSE. For solving Eqs. (1) and (2), following boundary conditions are used: $\psi = constant$ is prescribed on all the four walls of LDC to satisfy no-slip condition. The wall vorticity is given exactly as, $\omega_b = -\frac{\partial^2 \psi}{\partial n^2}$, where n is the wall-normal coordinate chosen for the four segments of the cavity. The wall vorticity, ω_b , is calculated using Taylor's series expansion at the walls with appropriate velocity conditions at the boundary segments. The top lid moves horizontally with a unit nondimensional velocity to provide the lead truncation error in calculating ω_b as $\frac{\Delta n}{3} \frac{\partial \psi}{\partial n^3}$. In Fig. 2, we show variation of ω_b with x for the top lid, which shows the maximum amplitude of wall vorticity to scale inversely with Δn . To solve the discretized Eq. (1), a fast and convergent elliptic PDE solver, Bi-CGSTAB method [29] has been used. The convection and diffusion terms of Eq. (2) are discretized using the CCD method [11–13] to obtain

both first and second derivatives, simultaneously. The relevant details about CCD and other compact schemes have been discussed in Ref. [30]. For time advancing Eq. (2), four-stage, fourth-order Runge-Kutta (RK4) method is used. The CCD scheme has been analyzed for resolution and effectiveness in discretizing the diffusion terms along with the dispersion relation preservation properties for 1D convection equation [11,12]. The CCD scheme with RK4 method has been characterized for convection-diffusion equation in Ref. [31] to show the importance of Peclet number. A nondimensional time-step of $\Delta t = 0.001$ is used to solve for the lower resolution grids, while the (1025×1025) grid uses $\Delta t = 0.0005$ for the computations reported here. For the finest grid used here, an even more refined time step of $\Delta t = 0.0001$ is used to counteract any adverse effects of such a refined grid due to expressing the diffusion operator via the Peclet number. It has been noted that the final limit cycle behaves in a similar fashion even though the time step is changed, the difference being only in the appearance of the instability of the limit cycle at different time ranges with change in Δt .

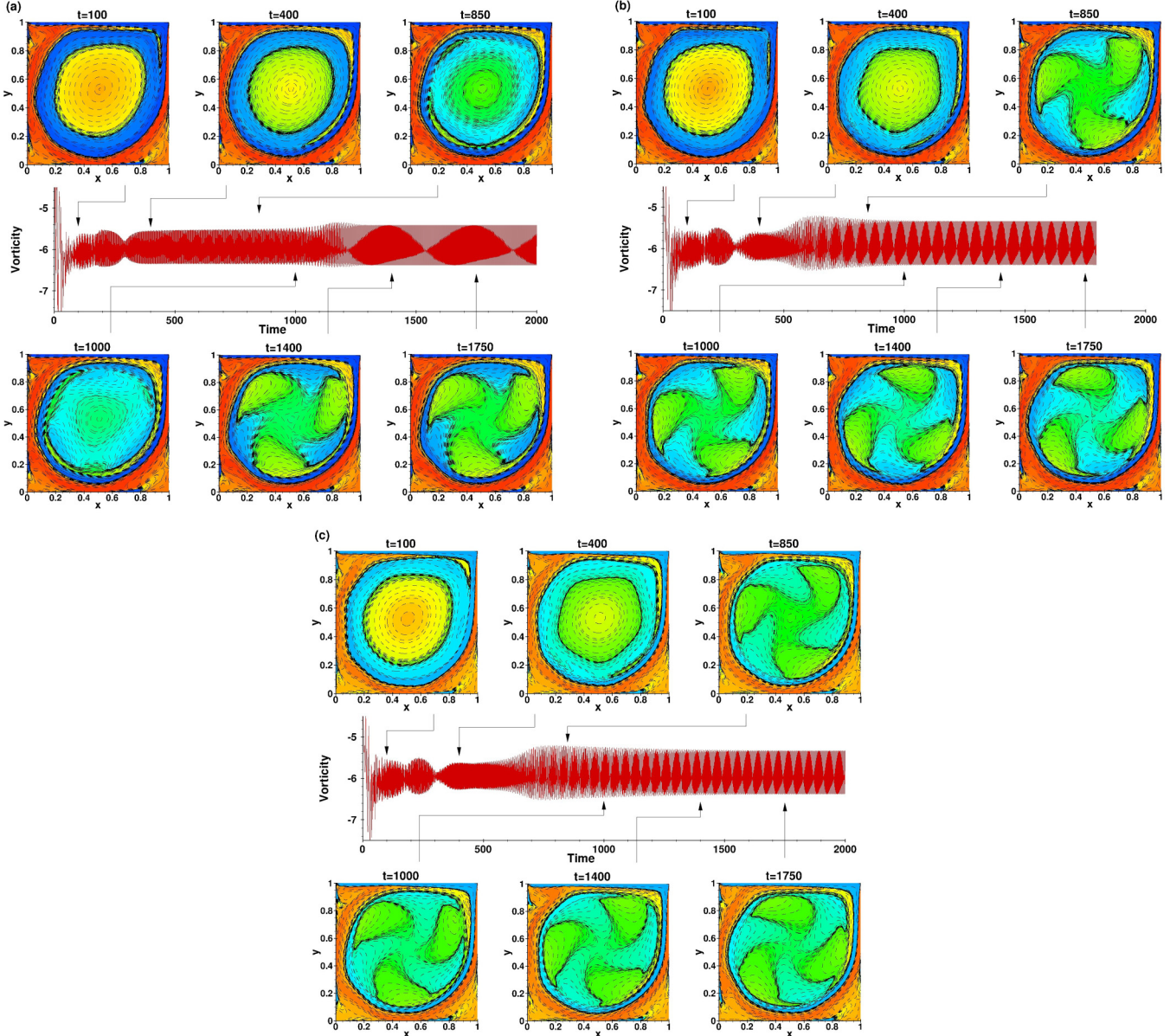


FIG. 5. Plot of vorticity time series and vorticity contours showing the dynamics of flow inside LDC at different times for $\text{Re} = 9600$ for (a) (257×257) , (b) (513×513) , and (c) (1025×1025) grids.

III. DYNAMICS OF SINGULAR LDC FLOW WITHOUT EXCITATION

The flow dynamics inside the LDC is presented for a super-critical $\text{Re} = 8750$ computed for the (257×257) grid in Fig. 3, with the help of vorticity time series sampled at $(x = 0.95, y = 0.95)$ (shown in the center). In the time series, identified various regimes are due to the different dynamics occurring during flow evolution. For example, in Range-1a in the time series, plotted vorticity displays high-frequency transient variations and is followed by banded relatively lower-frequency variations, identified as Range-1b. In this range, it is possible to see coherent vortices inside the cavity. However, such structures at the core are highly transient and the time series shows a decay of the signal near the terminal time of Range-1b, i.e., the vorticity fluctuation reduces till it settles down to a steady value. This steady state is maintained in Range-2. The flow

then suffers a temporal instability, evidenced by the growth of vorticity in Range-3. Finally, the flow attains a stable limit cycle oscillation stage, where one notices nonlinear saturation of the growing vorticity.

For the time series in Fig. 3, the linear growth in Range-3 is followed by nonlinear saturation, which has been modeled often by the Stuart-Landau equation [32]. An objective discussion on the applicability of this model is given in Refs. [17,33,34]. We remark that the results obtained by high-accuracy solution of time-dependent NSE in Range-2 and that obtained from solution of steady NSE do not match. Due to this, in the following linearly unstable range, solutions obtained by time-dependent NSE in Range-3 would also not necessarily be the same, which is obtained from the eigenvalue analysis of *steady* NSE solution. Also mismatch in Ranges-2 and -3 is due to differences in accuracy of numerical methods. Steady-state solution obtained often for very high

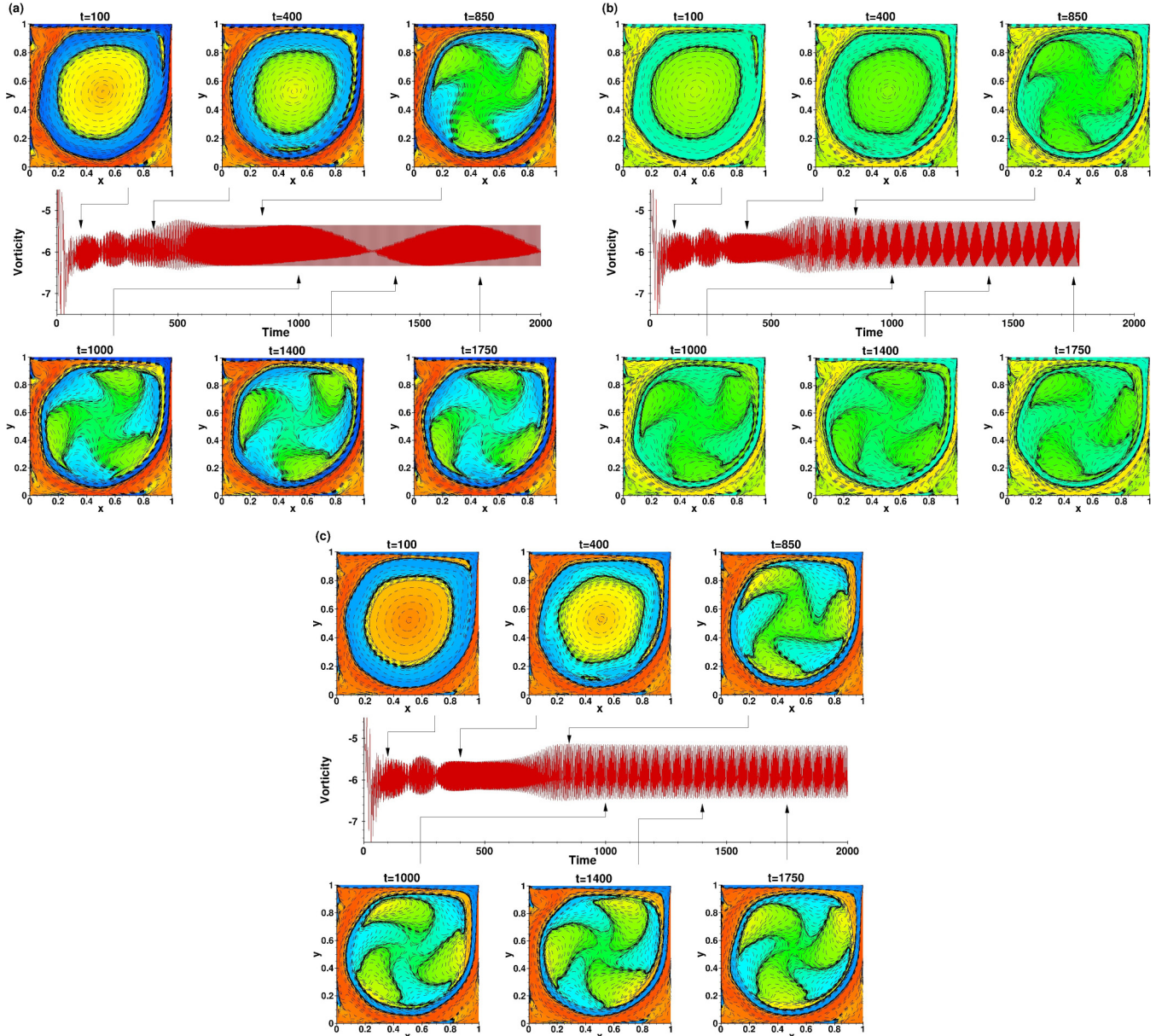


FIG. 6. Plot of vorticity time series and vorticity contours showing the dynamics of flow inside LDC at different times for $Re = 9700$ for (a) (257×257) , (b) (513×513) , and (c) (1025×1025) grids.

Re is due to the diffusive nature of numerical methods, as have been reported for $Re = 20\,000$ [24,25]. The sensitive dependence of the solution of a nonlinear dynamical system to initial condition (here the equilibrium states obtained in two ways) is well known and for flows governed by NSE is recorded in Ref. [30]. Eventually, the dynamical system settles down to a limit cycle for the time-dependent NSE solution.

Next, the flow dynamics inside the LDC is presented for a supercritical $Re = 9600$ obtained with the (1025×1025) grid in Fig. 4. Here, the flow does not attain a quiescent state (Range 2–3 in Fig. 3). Instead, a linear growth is observed after the initial vorticity fluctuations, which quickly attains saturation and decay as seen in the time between 200 and 300. After this period, the flow suffers an instability and nonlinear saturation during $t = 300$ and 500. At this stage the flow suffers a secondary instability, witnessed by a growth

and a multi-periodic nature during $t = 500$ and 1000. The amplitude envelope decays slowly with time and settles to a stable limit cycle oscillation beyond $t = 1750$. These results are obtained using the new parallelization strategy and it has been calibrated with the serial code for identical grids for a Reynolds number 10 000.

The flow dynamics is qualitatively similar using refined grid for supercritical Reynolds numbers ($Re \geq Re_{cr1}$) with the system suffering multiple Hopf bifurcations. It should be noted that Re_{cr1} is different for the two grids studied in Ref. [13]. This observation is further reinforced by the computations using (1025×1025) grid for which the flow becomes unsteady without any excitation at $Re (= Re_{cr1}) \approx 9530$. At Reynolds numbers below this, the flow is steady without any excitation. When an explicit excitation is applied to the system at subcritical Re , the flow suffers primary instability and

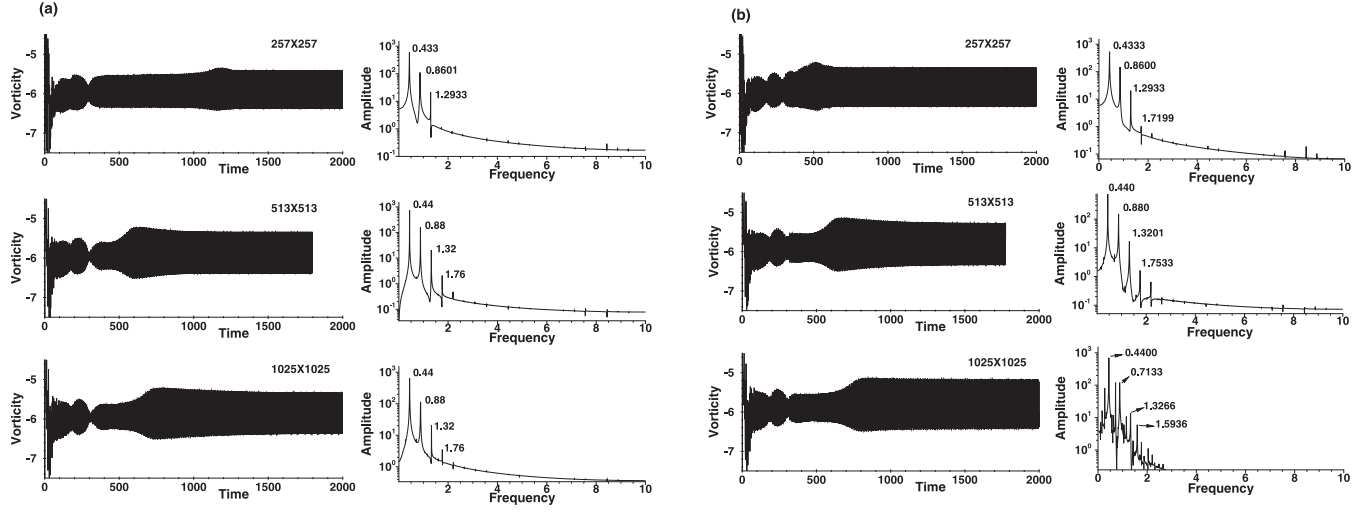


FIG. 7. Plot of vorticity time series obtained at location $(0.95, 0.95)$ and its corresponding FFT spectrum for (a) $Re = 9600$ and (b) $Re = 9700$.

displays a limit cycle above a threshold amplitude, even after the excitation is withdrawn. As Re_{cr1} for the (1025×1025) grid is higher compared to (257×257) and (513×513) grids, we present results for $Re = 9600$ and 9700 as the flow is unsteady for the all these three grids to study the grid sensitivity on the flow dynamics.

In Figs. 5 and 6, the vorticity field at different time instants are shown for the three grids for $Re = 9600$ and 9700 , respectively. Time series sampled at the point $(0.95, 0.95)$ are shown in the center of the figures. Different dynamics are noted for the grids during the initial and linear instability stages, as seen by comparing the frames at $t = 100$ and $t = 400$ for both the Reynolds numbers. One notes that the vorticity contours for the (257×257) grid are different from the other grids during this period. This is due to the dominance of aliasing error at the top lid boundary, as seen from Fig. 2. The finer grids with (513×513) and (1025×1025) show reduced aliasing error. One also notes from Fig. 2 that by refining the grid, progressively higher vorticity gradient is obtained at the top corners, $(\frac{\partial \omega}{\partial x})$, which will make the equilibrium flow somewhat different for different grids, leading to difference in dynamics. This may make the flow grid-dependent and can explain the grid sensitivity noted for computations with the relatively coarser grids with (257×257) and (513×513) points. We will revisit this aspect of grid dependence, with results shown for a more refined grid with (2049×2049) points. The difference in dynamics noted for the (257×257) grid is due to dominant aliasing error, which determines the dynamics by introducing spatiotemporal scales for the flow. However, for the (513×513) and (1025×1025) grids, aliasing error is reduced and absent, respectively, and the vorticity dynamics and bifurcation sequences are by Gibbs' phenomenon. We note in Fig. 5, a stronger secondary instability for the (1025×1025) grid (seen from the frame at $t = 400$), as compared to the coarser grids. One notes a distinct, pentagonal vortex at $t = 400$ for this grid. This is due to capturing fine spatial scales by the increased resolution of the grid and the localized nature of excitation from the top two corner points by Gibbs' phenomenon. One also notes the secondary

instability persisting for a longer time for this finer grid, as noted in the vorticity time series.

Further insights into grid sensitivity is obtained from Figs. 7(a) and 7(b), where vorticity time series and corresponding FFT are compared for the three grids. For $Re = 9600$, we see that the flow suffers a secondary instability at similar times for both the (513×513) and (1025×1025) grids, both the cases are not affected by aliasing error. For the (1025×1025) grid, the instability continues to persist for a longer time. However, for the (257×257) grid a delay is noted for the secondary instability, for which the effects of Gibbs' phenomenon will be the least. The corresponding FFT for the (513×513) and (1025×1025) grids are similar in terms of the structure and the number of peaks, while the (257×257) grid shows fewer peaks. Similar observations are noted for the secondary instability for $Re = 9700$ case. One also notes the multimodal nature of the time-series for the (1025×1025) grid. This is also reflected in the FFT plots which show the presence of multiple peaks for this case. This is because the flow bypasses the first two bifurcations for this finer grid. In Fig. 6 of Lestandi *et al.* [13], multiple Hopf bifurcations are noted for the LDC flow and it is shown that for (257×257) grid, a third bifurcation occurs at around $Re = 10500$.

IV. SUBCRITICAL INSTABILITY VIA FORCED EXCITATION

Simulations of unsteady NSE for LDC reported in Ref. [13] show the flow to remain steady for $Re < Re_{cr1}$. It is noted that the Re for which the flow becomes unsteady without any external excitation, is dependent on the grid, for which aliasing error is dominant. In Ref. [13], subcritical instability has been shown for both the (257×257) and (513×513) grids, where it is shown that the flow becomes unsteady when an external excitation by a pulsating vortex is applied. For certain amplitudes of excitation it is also reported [13] that the flow continues to remain unsteady after the withdrawal of excitation, showing self-sustained unsteadiness. This is demonstrated later, for the case of (1025×1025) grid for

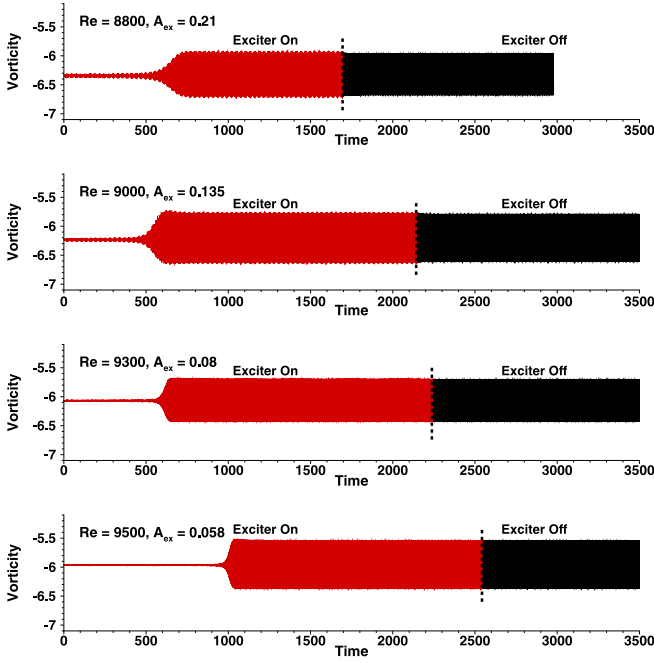


FIG. 8. Plot of vorticity time series at location $(0.95, 0.95)$ for the external vortical excitation imposed at $(0.02, 0.98)$ for subcritical Reynolds numbers. The results are for (1025×1025) grid and the amplitude of excitation is indicated by A_{ex} .

indicated subcritical Re values. The external vortical excitation used here is of the form, $\omega = A_{\text{ex}} \sin(2\pi f_o t)$ and is applied at the point $(0.02, 0.98)$ as shown in Fig. 8.

The reason for unsteadiness by subcritical instability caused due to imposed excitation is explained next. While the flow may admit instability, in the absence of excitation, the response of the dynamical system will only show the

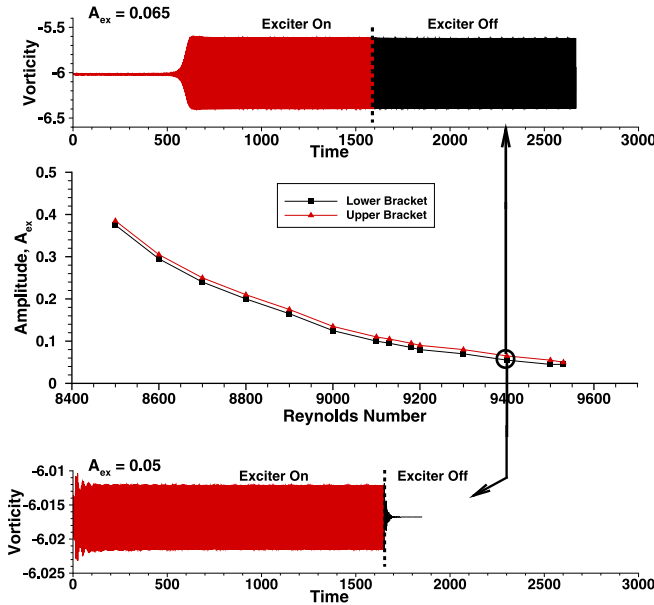


FIG. 9. Vorticity time series for $Re = 9400$ at the indicated excitation amplitudes and the band of threshold amplitude of vortical excitation for the (1025×1025) grid.

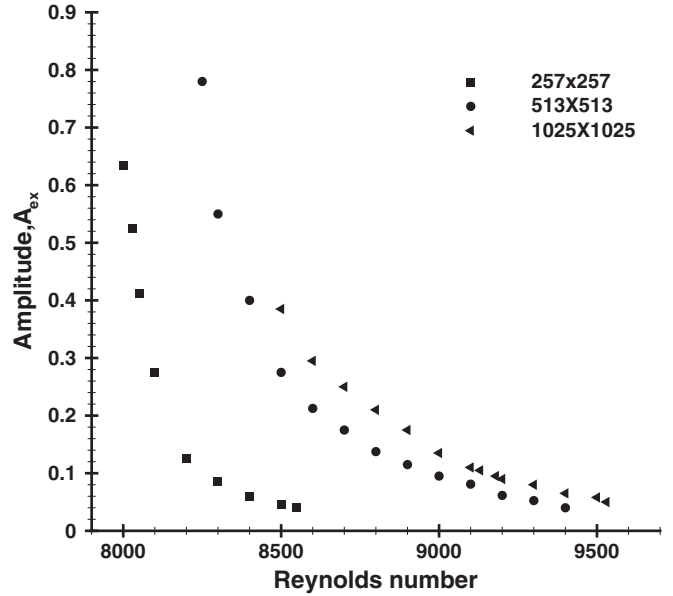


FIG. 10. Threshold amplitudes of pulsating vortical excitation needed for the three grids used here, having (257×257) , (513×513) , and (1025×1025) points.

equilibrium flow. Thus, any accurate method for LDC will not display unsteadiness, unless it is enforced explicitly or implicitly. For a neutrally stable numerical method, in the absence of implicit excitation by numerical errors, explicit excitation is required to make the flow unsteady for $Re \leq Re_{\text{cr}}$. For super-critical Re, unsteadiness is caused by implicit sources of numerical error. Existence of a Re_{cr1} for a numerical method implies that the existing numerical errors, including the Gibbs' phenomenon, for a subcritical Re is not adequate to excite physical instability. Thus for high-accuracy methods, it is possible to trigger subcritical instability via an external

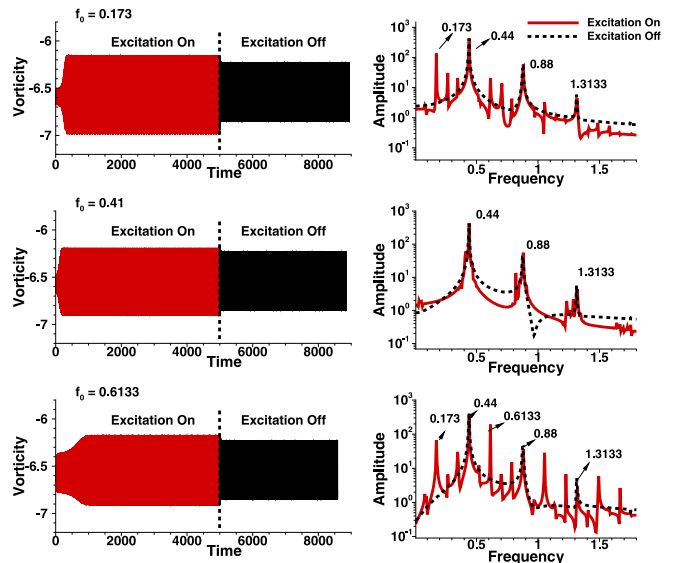


FIG. 11. Fast Fourier transform of the vorticity time series for $Re = 8500$ and amplitude of excitation $A_{\text{ex}} = 1$ for different excitation frequencies: $f_o = 0.173$, $f_o = 0.41$, and $f_o = 0.6133$, for 257×257 grid.

TABLE I. Natural frequencies and amplitudes for (1025×1025) grid.

Re	F ₁	F ₂	F ₃	F ₄
8500	0.4466 (792.41)	0.8909 (112.76)	1.3298 (6.32)	1.7662 (1.1797)
8600	0.4488 (818.24)	0.8912 (89.22)	1.3399 (7.12)	1.7709 (0.1791)
8700	0.4489 (558.21)	0.8908 (78.66)	1.3397 (9.58)	1.7863 (6.6108)
8800	0.4466 (1012.83)	0.8933 (132.01)	1.3410 (9.84)	1.784 (0.71755)
8900	0.4467 (1045.04)	0.8934 (128.67)	1.3330 (15.81)	1.7836 (2.0636)
9000	0.4466 (1040.57)	0.8867 (144.76)	1.3330 (21.98)	1.7865 (2.9502)
9100	0.4466 (1002.79)	0.8867 (199.46)	1.3333 (24.70)	1.7733 (1.9632)
9130	0.6199 (693.27)	1.2330 (30.23)	1.8533 (5.67)	2.4735 (0.6432)
9180	0.6199 (690.33)	1.2330 (35.98)	1.8533 (5.81)	2.4665 (1.5347)
9200	0.6199 (685.31)	1.2330 (37.01)	1.8534 (6.29)	2.4667 (1.5134)
9300	0.6133 (761.60)	1.2333 (37.66)	1.8466 (5.54)	2.4666 (1.5297)
9400	0.6133 (938.01)	1.2334 (45.07)	1.8467 (10.02)	2.4678 (1.9155)
9500	0.6136 (111.35)	1.2334 (35.13)	1.8467 (14.34)	2.461 (2.183)
9530	0.6133 (1164.22)	1.2266 (39.81)	1.8467 (11.01)	2.46 (0.592)
9580	0.4466 (1290.87)	0.8866 (235.35)	1.3267 (33.41)	1.7667 (6.0165)
9600	0.4467 (1042.69)	0.8867 (207.42)	1.3333 (30.69)	1.7733 (2.5189)
9650	0.4466 (1355.25)	0.7133 (273.16)	0.8867 (214.50)	0.273 (190.895)
9700	0.4415 (1402.38)	0.7166 (318.22)	0.8845 (253.11)	0.9865 (58.42)
9800	0.4412 (1396.35)	0.7134 (637.57)	0.8811 (260.11)	0.9865 (58.42)
9900	0.4401 (1334.84)	0.7133 (774.45)	0.8810 (228.92)	1.1533 (58.8711)
10 000	0.4400 (1251.31)	0.7133 (835.603)	0.88 (181.341)	0.5467 (172.383)

unsteady disturbance source for a certain range of Re below Re_{crl} . Further observations regarding the nature of excitation on subcritical instability can be drawn from Figs. 13 and 14 of Ref. [13], where unsteadiness is self-sustaining above a certain amplitude of the imposed external disturbances. Thus, there must exist a threshold value of the excitation amplitude above which the instability is self-sustaining and this is established next. We further establish that amplitude of vortical excitation is a primary variable, while frequency of excitation is not so, provided it is not too low.

A. Threshold amplitude of excitation for primary instability

In this section, we determine the threshold amplitude for subcritical Reynolds numbers computed for (257×257) , (513×513) , and (1025×1025) grids by a successive bracketing approach. Essentially, we identify a range of amplitudes, above which the excited unsteadiness is self-sustained (i.e., after the withdrawal of excitation), while below the lower limit of amplitude, the excited flow relaxes back to the unexcited state, when the external excitation is removed. Operationally, an equilibrium solution is obtained first for each grid for a chosen subcritical Re by solving the NSE until the solution becomes steady. This equilibrium flow is then subjected to the vortical excitation as defined earlier, for a pair of two different amplitudes, while the vorticity is monitored at the sampling point at $(0.95, 0.95)$. We denote the pair as $(A_{\text{ex},l}, A_{\text{ex},u})$, where $A_{\text{ex},l}$ is lower than $A_{\text{ex},u}$. When the vorticity time-series of the excitation cases reach a limit cycle state, excitation is switched off and the vorticity time series is monitored to check whether unsteadiness persists or not. If for the chosen $A_{\text{ex},l}$, the flow inside the LDC returns to its unexcited state, then this is chosen as an estimate for the lower bracket. Otherwise, the excitation amplitude is reduced and the vorticity time series

is monitored as before, for with and without the excitation sequence to locate the amplitude for which the switched-off condition reaches a quiescent state. Similarly, $A_{\text{ex},u}$ is also lowered, if the vorticity time-series shows sustained unsteadiness after removal of excitation. The excited flow is computed and the vorticity time series is monitored to check for sustained unsteadiness, when the excitation is switched off. This process is repeated, as long as the unsteadiness is noted to be self-sustaining, and any further reduction will quench the unsteadiness. This provides the threshold limit for $A_{\text{ex},u}$ above which the flow displays sustained unsteadiness for the excited cases. After determining the initial bracket, one can further refine the search for accurate threshold amplitude limits, as has been performed and shown in Fig. 9. We determine the threshold amplitude, while keeping the frequency of excitation as constant.

In Fig. 9, the threshold amplitude curve (center frame) is presented for the (1025×1025) grid, for different subcritical Re. In the center-frame, two curves are seen, with the upper curve corresponding to $A_{\text{ex},u}$, and the lower curve represents $A_{\text{ex},l}$, respectively. The corresponding vorticity time series at the sampling point for the upper and lower curves are demonstrated in the top and bottom panels of Fig. 9 for $Re = 9400$. It is clear that when the LDC is excited with an excitation amplitude $A_{\text{ex},l} = 0.05$, first the equilibrium flow is destabilized, and the flow field displays high vorticity fluctuations. This settles down to a stable limit cycle oscillation (LCO), after $t = 150$. However, on withdrawing the excitation, the vorticity fluctuations quickly decay to zero, as noted in the bottom frame of Fig. 9. For the excitation amplitude case with $A_{\text{ex},u} = 0.065$, the flow field continues to remain unsteady indefinitely after removal of excitation, as noted in the figure shown by dark lines. Two conclusions can be drawn from these threshold amplitude curves: (i) The instability is self-sustaining at

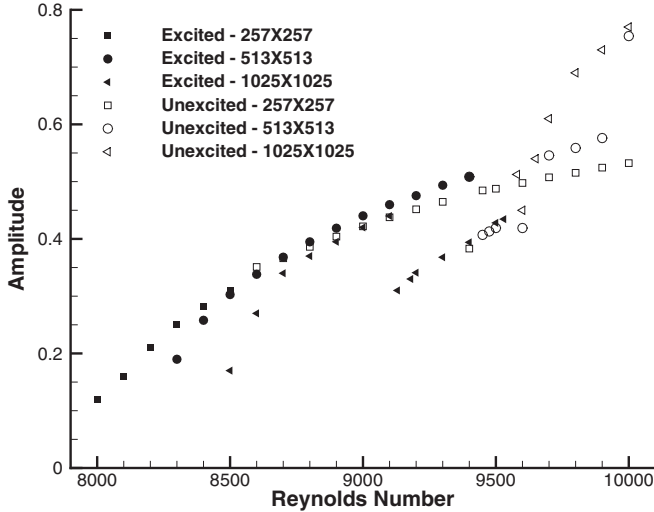


FIG. 12. Bifurcation diagram for the three grids with (257×257) , (513×513) , and (1025×1025) points.

and above the upper threshold amplitude, given by $A_{ex,u}$, and (ii) the upper and lower brackets are functions of Re .

It is easy to see in Fig. 9, that lower the subcritical Re , higher is the amplitude of excitation required for sustained unsteadiness, after removal of the source of excitation. Also the threshold amplitude decreases as Re is increased, due to higher receptivity of the flow at higher Re . Thus, the same numerical error present will cause the primary instability earlier for higher Re . When external excitation is superposed with the implicit numerical disturbances (including the Gibbs' phenomenon) of the computing method, the flow is even more receptive for unsteadiness via instability at lower imposed excitation amplitude.

The influence of grid resolution on $A_{ex,u}$ can be seen in Fig. 10, which is shown for the three grids. It is easily noted that at the same subcritical Re , the excitation amplitude is the lowest for the coarsest grid (257×257) , while it is the highest for the finer (1025×1025) grid. This supports the previous observation that the finer grid has lesser amount of numerical error to trigger instability, and hence the onset of unsteadiness is noted for higher Re with finer grid. This aspect of numerical errors along with Gibbs' phenomenon, provide the seed of instability and bifurcation is typical of this flow. It is noted that the threshold amplitude of imposed excitation is zero for the $Re_{cr1} = 9580$ for the (1025×1025) grid. This means that the (1025×1025) grid bypasses the first two bifurcations displayed by the (257×257) grid, which occurs at lower Re values.

B. Frequency spectrum of subcritical excitation

Response of LDC and its Strouhal number obtained by exciting the flow with three different frequencies ($f_o = 0.173$, 0.41 , and 0.6133) are shown in Fig. 11. The case is for $Re = 8500$, and the excitation amplitude used is $A_{ex} = 1$, which is same for all the cases. Results are obtained using the (257×257) grid and the spectrum of the vorticity time series are compared on the right-hand side of the frame, between the exciter-on and exciter-off cases. We note that for very low

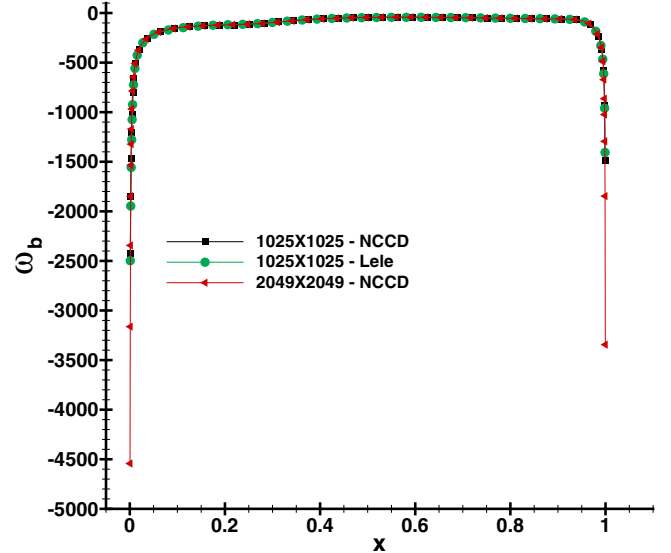


FIG. 13. Comparison of wall vorticity distribution at the top lid for $Re = 10000$ at $t = 1800$ — (1025×1025) and (2049×2049) grid points by using NCCD and Lele scheme.

exciting frequencies ($f_o \leq 0.01$), the flow is not receptive to vortical excitation, and the results are not shown. However, for $f_o > 0.02$, the flow exhibits a stable LCO following the primary instability. It is noted that the fundamental frequency of LDC is $f_N = 0.44$. Figure 11 shows three cases of excitation frequencies, and one observes the spectrum to be rich with higher harmonics of f_N and f_o , which is typical of nonlinear dynamical system showing multiple modes interacting. With increase in exciting frequency, the response field displays larger number of peaks. When the excitation is withdrawn, irrespective of different vortical exciting frequencies, the dynamical system attains stable LCO with $f_N = 0.44$ and its higher harmonics at $2f_N$, $3f_N$ and so on. The same behavior is noted for finer grids, although results are not shown, with the spectrum for different Re cases shown in Table I.

V. BIFURCATION DIAGRAM FOR DIFFERENT GRIDS

In Fig. 12, we have shown the bifurcation diagram for the three grids with (257×257) , (513×513) , and (1025×1025) points. This diagram contains information for all the cases, with and without any external excitation, to show similarities and differences with results presented specifically in Ref. [13]. Some of the salient features of the diagram are: (i) The flow with the coarsest grid (257×257) experiences bifurcations for $Re_{cr1} = 8030$ (with subcritical excitation), $Re_{cr2} \approx 9400$ and $Re_{cr3} \approx 10,500$; the grid with (513×513) points, the bifurcation begins at $Re_{cr1} = 8300$ (with subcritical excitation), and the next one occurs at $Re_{cr2} = 9450$ with another occurring at $Re_{cr3} \approx 9700$. The finer grid with (1025×1025) points exhibits $Re_{cr1} = 8500$ (with subcritical excitation) and the next one occurring for $Re_{cr2} \approx 9130$ (also with a subcritical excitation), while the last one noted without excitation is for $Re_{cr3} \approx 9580$. (ii) The reasons for obtaining different bifurcation sequences are due to the basic differences of the equilibrium flows, and the errors (including the Gibbs' phenomenon),

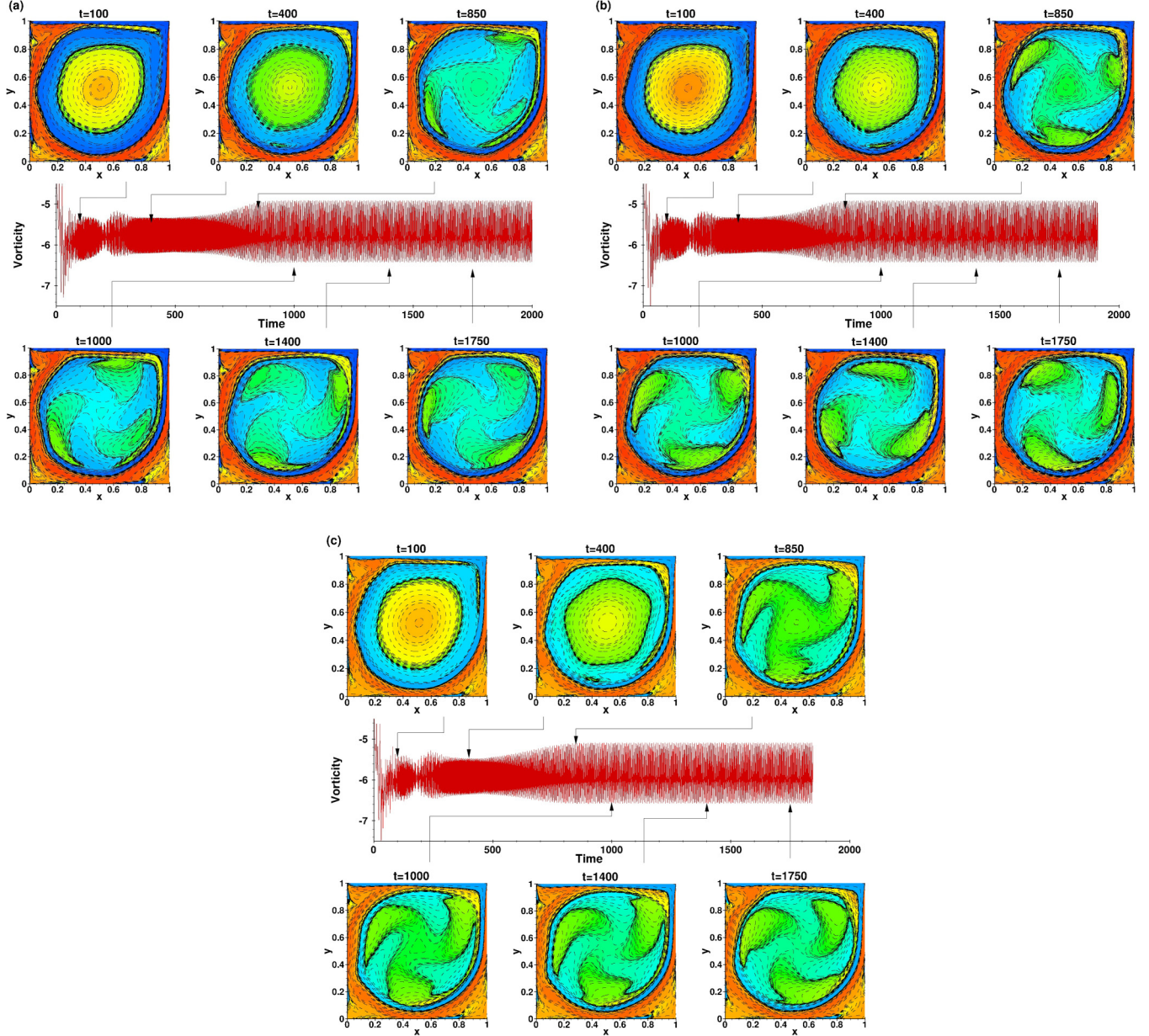


FIG. 14. Plot of vorticity time series and vorticity contours showing the dynamics of flow inside LDC at different times for $Re = 10\,000$ for (a) (1025×1025 —NCCD Scheme), (b) (1025×1025 —Lele Scheme), and (c) (2049×2049 —NCCD Scheme).

which triggers the instability. (iii) For the grids, we note equilibrium amplitudes to visit a branch from $Re \approx 9100$ to 9530 with lower amplitudes, as compared to the amplitude outside this range. (iv) Considering subcritical excitation, all the three grids show almost identical amplitudes of the LCO in the range: $8700 \leq Re \leq 9100$, showing the relevance of subcritical excitation. (v) We also note that in none of the grids, the bifurcation amplitudes start smoothly from $A_e = 0$, even when subcritical excitation is considered to initiate instability.

VI. TOWARD GRID-INDEPENDENCE AND UNIVERSALITY

We have noted the typical features of LDC flows over a period time, mostly using NCCD scheme [11–13,17,33], which

have not been reported before in computations. However, the presence of polygonal core vortex and specifically triangular vortex has been known to be created in laboratory experiments in Refs. [35,36]. Such polygonal structures have been noted in the atmosphere, above the north pole of Saturn in Ref. [37]. Any shear-driven confined flow can produce such polygonal structures. However, such structures in LDC flow have been reported mostly using combined compact difference scheme, although some other researchers using different methods have also reported triangular core vortex in Refs. [38,39]. To show that the polygonal vortex is not so difficult to obtain, here we show some results using Lele's compact scheme [40] in the parallel version for $Re = 10\,000$.

The main reason that Lele's scheme has been used rarely is due to the fact that compact schemes require boundary

closure schemes, and the ones proposed in Ref. [40] produces antidi diffusion [30,41] and leads to solution blow-up due to numerical instability, especially for internal flows. This issue of antidi diffusion causing numerical instability is common with compact schemes, and has been shown and solution provided in Refs. [30,41]. When one such solution was used with Lele's scheme in a (257×257) grid, the solution blew up due to aliasing error and results are recorded in Ref. [30]. In the present exercise, we have therefore used a refined grid with (1025×1025) points to avoid aliasing problem without any specific dealiasing technique. The success of Lele's scheme is due to better boundary closure scheme, along with a refined grid used. Also to show the effects of grid-independence, we also have run another case using NCCD scheme with (2049×2049) grid-points.

In Fig. 13, we plot the wall vorticity at the top lid comparing the three cases for $Re = 10\,000$, at $t = 1800$. It is readily apparent that the vorticity variation in the interior points is identical. We have already noted that for LDC flow, the symmetry of the geometry and the ninety degree bend at the corners demands that the vorticity at these corner-points must be equal to zero, following the kinematic definition of vorticity, derived from the stream function value being constant on the wall. However, immediate points on either side of the corners will have nonzero wall vorticity. As the wall-vorticity value is determined by the grid spacing at the wall, one can expect this quantity to be the same for Lele's scheme and NCCD scheme using identical number of grid points. We also note that the wall vorticity will not be symmetric about the mid-plane, as the top lid motion will contribute to asymmetry, as noted in Fig. 13. One also notes that the finest grid used here with (2049×2049) points will have highest value of wall vorticity at the second, and the second-to-last points, which are also near to the respective wall. This behavior of wall vorticity taking larger values with grid refinement is an attribute of impulsive start, and there is no theoretical upper limit to this value. These large values at the second and second-to-last point for the wall-vorticity is responsible for the Gibbs' phenomenon becoming stronger and stronger with grid refinement. Thus, refining the grid reduces aliasing error, while it increases the adverse effects of Gibbs' phenomenon described for compact schemes in capturing shocks and discontinuity [42].

In Fig. 14, vorticity contours are plotted for the three cases for $Re = 10\,000$ and shown at the indicated times. The vorticity time series at the sampling point is shown in the center of the clusters for all the three cases. As noted earlier, following the primary instability, during the LCO one notices the polygonal core vortex, which happens to be a pentagonal vortex for these refined grids at $t = 400$. The pentagonal vortex morphs into a triangular vortex, when the primary LCO suffers secondary instability, as shown in the frame for $t = 850$. Presence of the polygonal vortex for both the refined grid, indicates the grid-independence of the flow topology for these grids. Only notable differences at different frame can be related to effects of dispersion being responsible for the time-shift of identical events, with respect to each other.

In Fig. 15, the spectrum of the time series shown in Fig. 14 are shown, which show a very strong similarity among the three plots, specifically, between the NCCD and

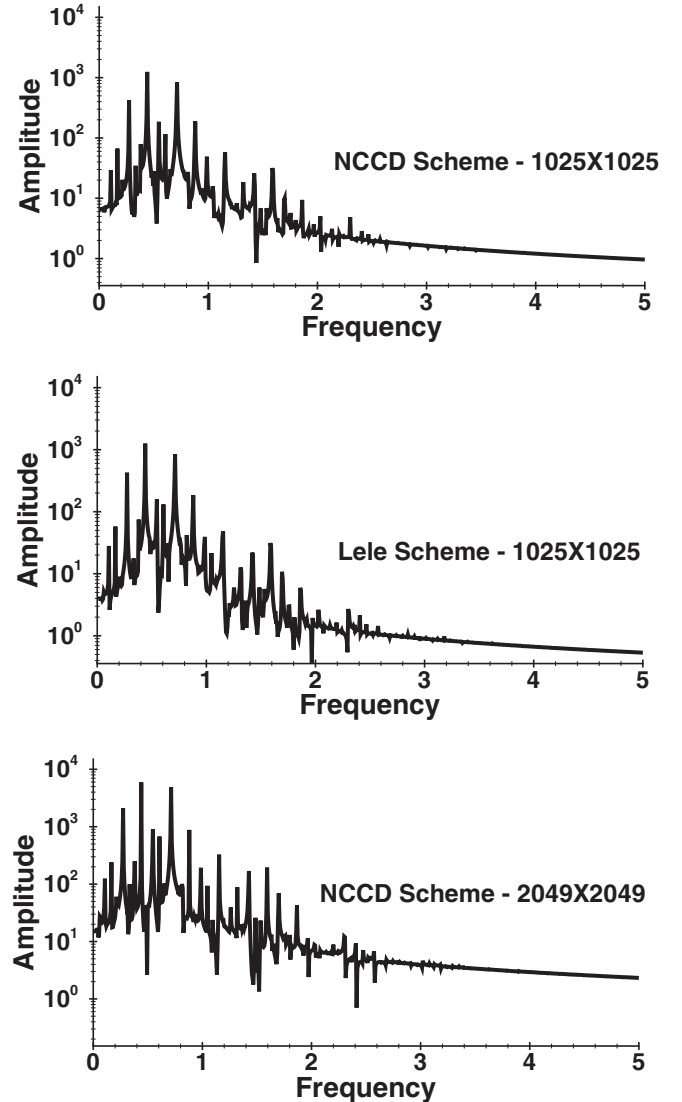


FIG. 15. Fourier transform of vorticity time series for $Re = 10\,000$ using two grids: (1025×1025) and (2049×2049) with NCCD and Lele's schemes.

Lele's schemes used with (1025×1025) grid. The five dominant modes are given in Table II, and the tabulated values clearly indicate the strength of the peaks to become progressively stronger due to increasing severity of Gibbs' phenomenon [42] due to grid refinement. One notes that physical Gibbs' phenomenon can be of different magnitude, from the

TABLE II. Leading natural frequencies and amplitudes for the two methods using the displayed grid.

Frequency	NCCD (1025×1025)	Lele (1025×1025)	NCCD (2049×2049)
F_1	0.440 (1619.60)	0.440 (1631.39)	0.440 (7908.77)
F_2	0.710 (1023.16)	0.709 (1033.6)	0.715 (4240.39)
F_3	0.275 (378.13)	0.275 (383.80)	0.270 (1719.27)
F_4	0.545 (259.09)	0.545 (249.47)	0.545 (1280.19)
F_5	0.880 (231.16)	0.880 (221.38)	0.880 (1227.21)

numerical one, which depends on grid refinement. However, as is typical of any other bluff body flows, universality is defined in terms of Strouhal number [17,34], and that is clearly noted in Fig. 15 and Table II. Interestingly, the Strouhal number in this case is given by the frequency value of 0.440, whose first superharmonic is noted as the fifth dominant mode. As one noted for coarser grid in Ref. [30], here also the spectrum of results for Lele's scheme shows wider band with peaks at higher frequencies, which are not present for the NCCD scheme, with both the grids.

VII. SUMMARY AND CONCLUSION

We summarize the major observations of the present research as follows: (i) The comparative study performed here displays the basic fact that the bifurcation sequences are universal with respect to the dominant frequency, as is usually the case for vortex-dominated flows [17,34]. This is clearly established in Fig. 15 and Table II, where we have also shown results for a finer grid with (2049×2049) points. (ii) We have shown the effects of various sources of errors, namely, the aliasing error and error introduced due to Gibbs' phenomenon. Of course, one has to account for truncation errors, which becomes significantly lower for the used compact schemes. Moreover, the reported computations are for extra-refined grids using (1025×1025) and (2049×2049) points, which have not been shown before. (iii) The reason for the differences among the different grid cases is due to differences in the equilibrium flow initiated by the created vorticity on the top wall, which is highlighted in Figs. 2 and 13. Finer grids experience larger discontinuous jumps at the corners of the top lid causing the Gibbs' phenomenon. The source of error is qualitatively different for the coarsest grid with (257×257) points, which experiences visible aliasing error. We note that by regularizing the corner singularities, a significantly higher $Re_{crl} = 10\,000$ to $10\,500$ have been reported earlier [26],

which can control both aliasing error and Gibbs' phenomenon. This is explained here for the first time. For the refined grid, one notices pentagonal core vortex for the (1025×1025) and (2049×2049) grids, which subsequently morphs into a triangular vortex, shown in Figs. 5, 6, and 14. Whereas, the (257×257) grid is known to support only a triangular core vortex in transient state. (iv) For all the grids, one notices a range of Re for which the flow displays self-sustained unsteadiness caused by imposed monochromatic excitation inside the domain, which does not disappear, when the excitation is switched off. This necessitates defining a threshold amplitude for the observed phenomenon in Figs. 8 and 9. (v) The effects of grid sensitivity for different refinements is reflected in the requirement of different threshold amplitudes of subcritical excitation for self-sustained unsteadiness displayed in Fig. 10. (vi) The dynamics is noted to be independent of frequency of excitation for a given grid, as shown in Fig. 11 for the coarsest grid. (vii) As noted before [13], one notices instability of LCO for all the three grids, as shown in Figs. 3–6 and 14. (viii) The subcritical excitation cases shown in Table I and Figs. 8 and 11, suggest the possibility of finding the natural frequency of the fluid dynamical system, by exciting the system at a frequency with sufficient amplitude and then removing the excitation after the LCO attains a steady state. Thereafter, the dynamical system displays self-sustained LCO at its natural frequency. Present study of nonlinear dynamics of flow in LDC is based on high-accuracy parallel computing of Navier-Stokes equation, which show delay of bifurcation as the grid is refined. There is another novel approach of studying the same flow by variations of lattice Boltzmann method (LBM) [43], which display numerical instability at Reynolds number which is significantly lower than that is reported using solution of Navier-Stokes equation. As these LBMs are very fast, it would be interesting to see refinement of the methods with results being in conformity with the present high-accuracy approach

-
- [1] P. G. Drazin and W. H. Reid, *Hydrodynamic Stability* (Cambridge University Press, Cambridge, UK, 1981).
 - [2] T. K. Sengupta, *Instabilities of Flows and Transition to Turbulence* (CRC Press, Boca Raton, FL, 2012).
 - [3] S. Bhaumik and T. K. Sengupta, Precursor of transition to turbulence: Spatiotemporal wave front, *Phys. Rev. E* **89**, 043018 (2014).
 - [4] S. Bhaumik and T. K. Sengupta, Impulse response and spatiotemporal wave packets: The common features of rogue waves, tsunami and transition to turbulence, *Phys. Fluids* **29**, 124103 (2017).
 - [5] P. Huerre and M. Rossi, Hydrodynamic instabilities in open flow, in *Hydrodynamic and Nonlinear Instabilities*, edited by C. Godrèche and P. Manneville (Cambridge University Press, Cambridge, UK, 1998).
 - [6] F. Auteri, L. Quartapelle, and L. Vigevano, Accurate ω - ψ spectra: Solution of the singular driven cavity problem, *J. Comput. Phys.* **180**, 597 (2002).
 - [7] O. Botella and R. Peyret, Benchmark spectral results on the lid-driven cavity flow, *Comput. Fluids* **27**, 421 (1998).
 - [8] O. R. Burgraff, Analytical and numerical study of the structure of steady separated flows, *J. Fluid Mech.* **24**, 113 (1966).
 - [9] U. Ghia, K. N. Ghia, and C. T. Shin, High-Re solutions for incompressible flow using the Navier-Stokes equations and a multigrid method, *J. Comput. Phys.* **48**, 387 (1982).
 - [10] R. Schreiber and H. B. Keller, Driven cavity flows by efficient numerical techniques, *J. Comput. Phys.* **49**, 310 (1983).
 - [11] T. K. Sengupta, V. Lakshmanan, and V. V. S. N. Vijay, A new combined stable and dispersion relation preserving compact scheme for non-periodic problems, *J. Comput. Phys.* **228**, 3048 (2009).
 - [12] T. K. Sengupta, V. V. S. N. Vijay, and S. Bhaumik, Further improvement and analysis of CCD scheme: Dissipation discretization and de-aliasing properties, *J. Comput. Phys.* **228**, 6150 (2009).
 - [13] L. Lestandi, S. Bhaumik, G. R. K. C. Avatar, M. Azaiez, and T. K. Sengupta, Multiple Hopf bifurcations and flow dynamics inside a 2D singular lid driven cavity, *Comput. Fluids* **166**, 86 (2018).

- [14] J. W. Goodrich, K. Gustafson and K. Halasi, Hopf bifurcation in the driven cavity, *J. Comput. Phys.* **90**, 219 (1990).
- [15] K. Gustafson and K. Halasi, Vortex dynamics of cavity flows, *J. Comput. Phys.* **64**, 279 (1986).
- [16] T. Osada and R. Iwatsu, Numerical simulation of unsteady driven cavity flow, *J. Phys. Soc. Jpn.* **80**, 094401 (2011).
- [17] T. K. Sengupta, N. Singh, and V. V. S. N. Vijay, Universal instability modes in internal and external flows, *Comput. Fluids* **40**, 221 (2011).
- [18] T. K. Sengupta, A. Dipankar, and K. A. Rao, A new compact scheme for parallel computing using domain decomposition, *J. Comput. Phys.* **220**, 654 (2007).
- [19] R. Seydel, *Practical Bifurcation and Stability Analysis from Equilibrium to Chaos* (Springer, Berlin, 1994).
- [20] F. Auteri, N. Parolini, and L. Quartapelle, Numerical investigation on the stability of singular driven cavity flow, *J. Comput. Phys.* **183**, 1 (2002).
- [21] M. Sahin and R. G. Owens, A novel fully-implicit finite volume method applied to the lid-driven cavity problem. Part II. Linear stability analysis, *Int. J. Num. Meth. Fluids* **42**, 79 (2003).
- [22] W. Cazemier, R. W. C. P. Verstappen, and A. E. P. Veldman, Proper orthogonal decomposition and low-dimensional models for driven cavity flows, *Phys. Fluids* **10**, 1685 (1998).
- [23] C. H. Bruneau and M. Saad, The 2D lid-driven cavity problem revisited, *Comput. Fluids* **35**, 326 (2006).
- [24] V. B. L. Boppana and J. S. B. Gajjar, Global flow instability in a lid-driven cavity, *Int. J. Num. Meth. Fluids* **62**, 827 (2010).
- [25] E. Erturk, T. C. Corke, and C. Gökcöl, Numerical solutions of 2-D steady incompressible driven cavity flow at high Reynolds numbers, *Int. J. Num. Meth. Fluids* **48**, 747 (2005).
- [26] J. Shen, Hopf bifurcation of the unsteady regularized driven cavity flow, *J. Comput. Phys.* **95**, 228 (1991).
- [27] M. Poliashenko and C. K. Aidun, A direct method for computation of simple bifurcations, *J. Comput. Phys.* **121**, 246 (1995).
- [28] Y.-F. Peng, Y.-H. Shiau, and R. R. Hwang, Transition in a 2-D lid-driven cavity flow, *Comput. Fluids* **32**, 337 (2003).
- [29] H. A. Van der Vorst, Bi-CGSTAB: A fast and smoothly converging variant of Bi-CG for the solution of non-symmetric linear systems, *SIAM J. Sci. Stat. Comput.* **13**, 631 (1992).
- [30] T. K. Sengupta, *High Accuracy Computing Methods: Fluid Flows and Wave Phenomena* (Cambridge University Press, Cambridge, UK, 2013).
- [31] V. K. Suman, T. K. Sengupta, P. C. J. Durga, M. K. Surya, and D. Sanwalia, Spectral analysis of finite difference schemes for convection diffusion equation, *Comput. Fluids* **150**, 95 (2017).
- [32] J. T. Stuart, On the nonlinear mechanics of wave disturbances in stable and unstable parallel flows. Part 1. The basic behavior in plane Poiseuille flow, *J. Fluid Mech.* **9**, 353 (1960).
- [33] L. Lestandi, S. Bhaumik, T. K. Sengupta, G. R. K. C. Avatar, and M. Azaiez, POD applied to the numerical study of unsteady flow inside a lid driven cavity, *J. Math. Study* **51**, 150 (2018).
- [34] T. K. Sengupta, N. Singh, and V. K. Suman, Dynamical system approach to instability of flow past a circular cylinder, *J. Fluid Mech.* **656**, 82 (2010).
- [35] M. Beckers and G. J. F. Van Heijst, The observation of a triangular vortex in a rotating fluid, *Fluid Dyn. Res.* **22**, 265 (1998).
- [36] G. F. Carnevale and R. C. Koolsterziel, Emergence and evolution of triangular vortices, *J. Fluid Mech.* **259**, 305 (1994).
- [37] <https://www.firstpost.com/tech/science/nasas-cassini-finds-six-sided-vortex-in-atmosphere-above-saturn's-north-pole-5133671.html> (2018)
- [38] Y. G. Bhumkar, T. W. H. Sheu, and T. K. Sengupta, A dispersion relation preserving optimized upwind compact difference scheme for high-accuracy flow simulations, *J. Comput. Phys.* **278**, 378 (2014).
- [39] N. Sharma, A. Sengupta, M. K. Rajpoot, R. J. Samuel, and T. K. Sengupta, Hybrid sixth-order spatial discretization scheme for nonuniform Cartesian grids, *Comput. Fluids* **157**, 208 (2017).
- [40] S. K. Lele, Compact finite difference schemes with spectral-like resolution, *J. Comput. Phys.* **103**, 16 (1992).
- [41] T. K. Sengupta, G. Ganeriwal, and S. De, Analysis of central and upwind compact schemes, *J. Comput. Phys.* **192**, 677 (2003).
- [42] T. K. Sengupta, G. Ganeriwal, and A. Dipankar, High-accuracy compact schemes and Gibbs' phenomenon, *J. Sci. Comput.* **21**, 253 (2004).
- [43] A. Montessori, G. Falcucci, P. Prestininzi, M. La Rocca, and S. Succi, Regularized lattice Bhatnagar-Gross-Krook model for two- and three-dimensional cavity flow simulations, *Phys. Rev. E* **89**, 053317 (2014).